Case Studies in Thermal Engineering 63 (2024) 105338

Contents lists available at ScienceDirect

Case Studies in Thermal Engineering

journal homepage: www.elsevier.com/locate/csite

Numerical investigation on slip-flow and heat transfer characteristics in the entrance region of elliptical microchannels

Liangbin Su [a,b], Yongyi Yang [b], Liang Li [c,*], Wan Yu [a,b], Huashan Su [a,b], Gang Wang [a,b], Tao Hu [a,b,**]

[a] Hubei Key Laboratory of Hydroelectric Machinery Design & Maintenance, China Three Gorges University, Yichang, 443002, China
[b] College of Mechanical & Power Engineering, China Three Gorges University, Yichang, 443002, China
[c] College of Engineering Design and Physical Sciences, Brunel University London, Uxbridge, UB8 3PH, United Kingdom

ARTICLE INFO

Keywords:
Elliptical microchannels
Entrance region
Rarefaction effect
Axial heat conduction

ABSTRACT

This paper concentrates on the numerical investigation of slip-flow and heat transfer characteristics in the entry region of elliptical microchannels under isothermal or isoflux boundary conditions. Slip boundaries caused by rarefaction effect are implemented using user-defined functions. The impacts of Reynolds number ($25 \leq Re \leq 1000$), Knudsen number ($0.01 \leq Kn \leq 0.1$), Peclet number ($17.5 \leq Pe \leq 700$) and aspect ratio ($0.2 \leq \varepsilon \leq 1$) on the apparent friction factor Reynolds number product $f_{app}Re$ and local Nusselt number $Nu(x)$ are discussed in detail. The results demonstrate that at the entrance region, $f_{app}Re$ decreases with increasing Re, especially for $\varepsilon = 0.33$, $Kn = 0.01$ and $Re < 500$. However, it is independent of Re at fully developed region. At $\varepsilon = 0.75$ and $x^* = 0.0001$, when Pe ranges from 17.5 to 350, $Nu(x)$ is decreases by 87 % at the T boundary. The value of $Nu(x)$ for $Kn = 0.04$ is reduces by 333 when compared with no-slip case at Pe is 17.5. These indicate that heat transfer near the inlet can be effectively enhanced by axial heat conduction. While rarefaction reduces friction losses and weakens the effect of axial heat conduction. Generalized correlations are proposed for fully developed Nu.

Nomenclature

a	semi- major axis of the channel, m	x^*	dimensionless axial position
b	semi- minor axis of the channel, m	y	y-coordinate, m
c_p	specific heat, J/(kg·K)	z	z-coordinate, m
D_h	hydraulic diameter, m	Greek symbols	
Eu	Euler number	α	thermal diffusivity, m^2/s
f	friction factor	γ	specific heat ratio
F	tangential momentum accommodation coefficient	θ	dimensionless temperature
F_t	thermal accommodation coefficient	λ	gas mean free path, m
h	convective heat transfer coefficient, W/(m^2·K)	μ	fluid dynamic viscosity, kg/(m·s)
H	height of the microchannel heat sink, m	ε	aspect ratio, b/a
k	thermal conductivity, W/(m·K)	τ	wall shear stress, N/m^2

(*continued on next page*)

* Corresponding author. College of Engineering Design and Physical Sciences, Brunel University London, Uxbridge, UB8 3PH, United Kingdom.
** Corresponding author. College of Mechanical & Power Engineering, China Three Gorges University, NO. 8 University Road, Yichang, 443002, Hubei, China.

E-mail addresses: liang.li@brunel.ac.uk (L. Li), hutao@ctgu.edu.cn (T. Hu).

https://doi.org/10.1016/j.csite.2024.105338
Received 18 July 2024; Received in revised form 5 October 2024; Accepted 22 October 2024
Available online 28 October 2024

(*continued*)

Kn	Knudsen number	Subscripts	
L	length of the microchannel heat sink, m	app	apparent
Nu	Nusselt number	i	inlet
p	pressure, N/m^2	s	slip condition
Pe	Peclet number	m	mean
Pr	Prandtl number	w	wall
Po	Poseuille number	n	nondimensional
q''	heat flux, W/m^2	T	T boundary condition
Re	Reynolds number	H2	H2 boundary condition
S	cross-sectional area, m^2	ps	pseudo
T	temperature, K	Acronyms	
u	fluid velocity, m/s	AHC	axial heat conduction
Un	dimensionless velocity	FDR	fully developed region
W	width of the microchannel heat sink, m	2D	two-dimensional
x	x-coordinate	3D	three-dimensional
x^+	dimensionless axial flow distance		

1. Introduction

Research on microchannels dates back to the 1980s [1], and since then, investigations into microscale fluid flow and heat transfer have burgeoned. Due to rapid advancements in micro-manufacturing technology, microchannels have shown broad application prospects in biomedicine, chemical separation, energy, and other fields. Consequently, microfluidics has become a prominent research area [2–4]. An in-depth understanding of fluid flow and heat transfer performances in microchannels is significant for expanding their application scope.

Currently, the size of microchannel is not clearly defined. Microchannels are usually defined as channels with characteristic dimensions between 1 μm and 1 mm [5]. Typical applications may involve feature sizes range of about 10–200 μm [6,7]. Microchannel refers to the channel whose feature size is less than 1 mm. The force analysis in such tiny channels different from that in a macro channel, as surface tension, gravity, and fluid viscous forces become significant and cannot be ignored [8–10]. The validity of the continuity assumption is doubtful in some microscale fluid and thermal transport problems [11,12], particularly in the gas flow. The rarefaction effect due to less molecular collision is one of the main factors. This effect is commonly quantified using the Knudsen number *Kn*, which is defined as the ratio of the average free path of a gas molecule to the hydraulic diameter of the pipe. The fluid flow is classified as rarefied-flow for a range of *Kn* from 0.001 to 0.1 [13]. For gas flow in such microchannels or microtubules, the no-slip boundary condition is inappropriate, and a modified boundary condition, for instance the velocity-slip and temperature-jump on the wall, is essential to consider.

In recent decades, investigation of flow and heat transfer mechanisms in microchannels with common cross-section shapes has received extensive attention. Among the various flow patterns observed in microchannels, laminar flow stands out as the most common, and it can be further categorized into the entry and fully developed regions based on its extent of development. Renksizbulut et al. [14] analyzed the entry section of a rectangular microchannel with T boundary condition (constant axial and peripheral wall temperatures), focusing on the rarefied gas. They found that the friction factor *f* and Nusselt number *Nu* decreased greatly owing to the influence of rarefaction effect, especially in the entry section. Avramenko et al. [15] studied the start-up slip flow induced by sudden time-dependent pressure drop in a rectangular microchannel, and found that the increase of Knudsen number *Kn* prolonged the time for the flow to reach full development state, and the aspect ratio affected the flow stability time. Then, they [16] used the Fourier method and the method of the eigenfunction decomposition to investigate the slip flow characteristics in a curved microchannel with rectangular cross-section and found that increasing the radius of curvature radius will magnify the asymmetry of the velocity jump value at the channel wall. For slip gaseous flow at the inlet of parallel plates and circular microchannels, Duan and Muzychka [17] proposed a semi-theoretical model for forecasting $f_{app}Re$ with a precision of about 10 %. Su et al. [18] investigated circular and parallel plate microchannels with velocity-slip and temperature-jump applied at the wall under slip-flow regime. They developed correlations to estimate friction factors and local Nusselt number $Nu(x)$ of no-slip case. A finite-volume approach was employed by Aydin and Avci [19] to explore the influences of *Kn*, Peclet number *Pe*, and Brinkman number *Br* on the heat transfer in the entry section of a microtube with variable heat flux in the axial direction. They indicated that increasing the dimensionless heat flux decreases the average Nusselt number. Then they used the same method to further investigate the heat transport characteristics of forced convective thermally developing in a microtube with constant heat flux [20]. The study showed that the fully developed *Nu* is unaffected by *Pe*. In addition, Mohammed et al. [21] and Wang [22] also pointed out that the Poseuille number *Po* and *Nu* are significantly affected by velocity-slip and temperature-jump, and Wang [22] gave an exact analytical solution for fully developed *Nu* of slip-flow regime in a rectangular microchannel under H1 boundary condition (constant axial wall heat flux and peripheral wall temperature). Nemati et al. [23] performed a numerical investigation for multi-layer rectangular mini-channel heat sinks with simultaneously developing flow, presented an innovative analytical approach for calculating the base average temperature and, compared the results of this analytical method with those obtained from 2D and 3D simulations, discovering excellent consistent between the two. Additionally, they also derived correlations for the Nusselt number in these flows based on their simulation results.

Microchannels with unconventional geometric shapes, including trapezoidal [24,25], triangular [22,26], diamond [27,28] and elliptical [29,30] have increasingly garnered attention in recent times owing to their unique performances in fluid dynamics and heat transfer. Among these, elliptic channels have demonstrated higher heat transfer efficiency than circular tubes [31] and exhibit shape more consistent with aerodynamic design principles [32]. In general, the circular tube is also an elliptical channel with an aspect ratio of 1. Therefore, there has been a great interest in analyzing the flow and heat transfer of an elliptical microchannel. Shah and London [33] conducted a comprehensive review of previous studies and summarized earlier correlations for f and Nu of elliptical channels at the fully developed region (FDR). Duan and Muzychka [5] presented a model to anticipate Po of fully developed slip-flow for an oval microchannel. Nevertheless, an approximate assumption adopted in this model may cause some errors, particularly in microchannels with a low aspect ratio. Su et al. [30] eliminated the errors in Duan and Muzychka [5] by employing the binomial series twice and derived a new model for predicting Po, and the theoretical solutions agreed well with the numerical findings of Spiga and Vocale [34]. Vocale et al. [35] also analyzed the fully developed heat transfer characteristic in oval microchannels under H2 boundary condition (constant axial wall heat flux and uniform peripheral wall heat flux). They considered the rarefaction effect of gas and found that Nu decreases with the increase of Kn. Das and Tahouresi [36] employed integral transform techniques to examine the fully developed gaseous rarefied-flow for elliptical microchannel. They deduced an analytical solution and found that their results demonstrated good agreement with previous findings, with a maximum error of less than 0.2 %. Bhosale et al. [37] examined rarefied-flow and heat transfer of air for semicircular and elliptical microchannels. They discovered that for the same Re, the average Nu and f in the former were higher than that of the latter.

As aforementioned, the research on microchannels with various cross-sectional shapes has been extensive. But for elliptical microchannels, the existing work mainly focuses on the FDR, with limited studies on the inlet section. It is worth noting that compared to the FDR, the velocity and temperature distributions of elliptical microchannels change more dramatically in the entry section, rendering the flow and heat transfer characteristics particularly complex. Additionally, the entrance section accounts for the majority of shorter microchannels, making its impact on overall performance cannot be ignored. Su et al. [38] examined the entry region of oval minichannels, considering common three boundary conditions. However, it is for macro flow and ignores the significant rarefaction effect, namely, gaseous slip-flow, that is crucial in the microchannel. Hence, it is essential to conduct comprehensive and in-depth research on slip-flow and heat transfer characteristics at the entry section of the elliptic microchannels. Furthermore, the axial fluid heat conduction, despite being a critical effect in the entrance section, is frequently overlooked in macro channels for gases and liquids but plays a pivotal role in microchannel, often dominates the thermal transport for low Pe flow [39]. When axial heat conduction dominates, fluid and solid temperatures in the microchannel exhibit a noticeable nonlinear distribution [37,40] In the current work, the laminar flow and heat transfer characteristics of elliptical microchannels in the entrance region are studied numerically. The rarefaction and axial heat conduction are taken into account. The impacts of Re, Kn, Pe and ε on $f_{\mathrm{app}}Re$ and $Nu(x)$ are also analyzed in detail. The findings will offer meaningful insights into the design and optimization of heat exchangers using elliptic microchannels.

2. Model Description

2.1. Geometry of the microchannel

The schematic diagram of an elliptical microchannel heat sink is illustrated in Fig. 1. The length, width and height correspond to L, W and H, respectively. Air is chosen as the working fluid and the x-axis is set as the axial flow direction. In view of the symmetry principle, one-fourth of the elliptical channel is selected as the domain of numerical calculation, reducing computational complexity and time cost, as shown in Fig. 1(b).

2.2. Mathematical formulation

The numerical simulation is established using the following hypotheses: (1) the flow is 3D, steady laminar flow and incompressible; (2) considering velocity-slip and temperature-jump on the wall; (3) neglecting viscous dissipation and radiation heat transfer. Hence, according to these assumptions, the continuity, momentum, and energy equations are given as [38]:

$$\nabla \cdot \overrightarrow{U} = 0 \tag{1}$$

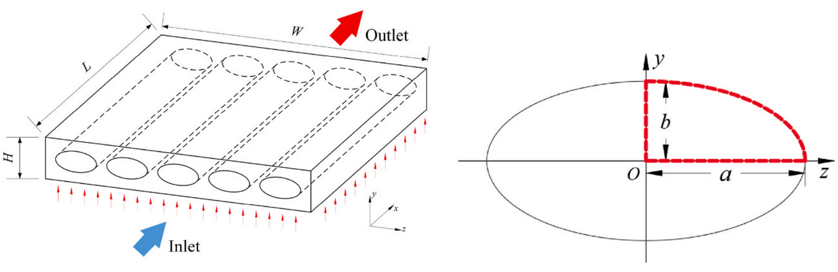

(a) (b)

Fig. 1. Schematic of the microchannel heat sink: (a) geometry model and (b) computational domain.

$$\rho\left(\vec{U}\cdot\nabla\vec{U}\right) = -\nabla p + \mu\nabla^2 U \tag{2}$$

$$\vec{U}\cdot\nabla T = \alpha\nabla^2 T \tag{3}$$

where ρ, p, μ, and α represent the density, pressure, fluid dynamic viscosity, and thermal diffusion coefficient, respectively.

For rarefied-flow, the Navier-Stokes equations remain work well when the flow satisfies the conditions for velocity-slip and temperature-jump at the walls [41]. To this end, the first-order boundary conditions [42] are adopted in this work, that is:

$$u_s = -\frac{2-F}{F}\lambda\frac{\partial u}{\partial n} \tag{4}$$

$$T_s - T_w = -\frac{2-F_t}{F_t}\frac{2\gamma\lambda}{(\gamma+1)Pr}\frac{\partial T}{\partial n} \tag{5}$$

where F and F_t denote the tangential momentum and thermal accommodation coefficients, respectively. The former, which usually varies between 0.87 and 1 [43] is set to unity. The latter is related to the surface material and specific gas. and for air, the coefficient is commonly treated as unity. λ is the mean free path of a gas molecule and γ refers to the specific heat ratio.

To simplify the calculation, the temperature-jump boundary condition was efficiently implemented by adopting a thermal resistance model proposed by Su et al. [18]. Eq. (5) can be converted to the following form:

$$h_{ps}(T_s - T_w) = -k\left(\frac{\partial T}{\partial n}\right) \tag{6}$$

where h_{ps} is a pseudo convective heat transfer coefficient and expressed as:

$$h_{ps} = \frac{kF_t(\gamma+1)Pr}{2\gamma KnD_h(2-F_t)} \tag{7}$$

The reciprocal of h_{ps} is the thermal resistance caused by the temperature jump boundary.

Furthermore, Eq. (6) can be transformed into the form of the third kind of boundary condition for surface convection heating [44].

$$h_{ps}\left(T_{f,ps} - T_{w,ps}\right) = q \tag{8}$$

where the wall temperature T_w can be regarded as $T_{f,ps}$, and the temperature of the fluid near the wall T_s can be regarded as $T_{w,ps.}$

Because the first and the second boundary conditions can be transformed into the third boundary condition. Therefore, for T boundary condition, the model only needs to set two constants without UDF (user-defined function). A simple UDF is sufficient to implement the temperature jump when combined with the thermal resistance model for H2 boundary condition.

For simultaneous developing flow, the inlet velocity is uniform. According to the continuity equation, the velocity is equal to the average velocity u_m of each cross-section. Note that the mean velocity is influenced by Reynolds number Re, that is:

$$u_m = \frac{\mu Re}{\rho D_h} \tag{9}$$

where D_h $(=\lambda/Kn)$, representing the hydraulic diameter of elliptical channels, ranges from 0.6 to 60 μm in this work.

To make the results clear, the following non-dimensional variables are introduced:

$$U_n = \frac{u}{u_m} \tag{10}$$

$$\theta_T = \frac{T - T_i}{T_w - T_i} \tag{11}$$

$$\theta_{H2} = \frac{T - T_i}{D_h q/k} \tag{12}$$

where U_n refers to the dimensionless velocity, θ denotes the dimensionless temperature, T_w represents the wall temperature, and T_i denotes the inlet temperature of the fluid. For T boundary condition, Eq. (11) is used, while Eq. (12) is for H2 boundary condition.

For the FDR, the Fanning friction factor f of a specified cross-section channel remains constant, which is expressed as [33]:

$$f = \frac{\tau}{(1/2)\rho u_m^2} \tag{13}$$

where τ denotes the wall shear stress.

To simplify the calculation of resistance in the inlet section, an apparent friction factor that comprehensively reflects both frictional resistance and entrance effects was defined by Shah and London [33].

$$f_{\text{app}} = \frac{\Delta p}{2\rho u_{\text{m}}^2} \frac{D_h}{x} \tag{14}$$

The apparent friction factor Reynolds number product $f_{\text{app}}Re$ is calculated by utilizing the pressure drop along the axial location, as represented in Eq. (15).

$$f_{\text{app}}Re = \frac{\Delta p}{2\rho u_{\text{m}}^2 x^+} \tag{15}$$

where x^+ denotes the dimensionless axial flow distance. It is defined as:

$$x^+ = \frac{x}{D_h Re} \tag{16}$$

where x is the local position of the streamwise direction.

The local convective heat transfer coefficient $h(x)$ in the channel is given by:

$$h(x) = \frac{q''}{T_{\text{w}}(x) - T_{\text{m}}(x)} \tag{17}$$

where q'' denotes the wall heat flux, $T_{\text{m}}(x)$ represents the mass-weighted average temperature defined as:

$$T_{\text{m}}(x) = \frac{\int_S T(y,z)u(y,z)dS}{\int u(y,z)dS} \tag{18}$$

In general, the heat transfer characteristics are described using the local Nusselt number, which is expressed as:

$$Nu(x) = \frac{h(x)D_h}{k} = \frac{q''(x,y,z)D_h}{k(T_{\text{w}}(x) - T_{\text{m}}(x))} \tag{19}$$

The dimensionless axial position for the thermal entrance region is obtained as follows:

$$x^* = \frac{x}{D_h RePr} \tag{20}$$

where $Pr = 0.7$ for all cases in this work.

2.3. Numerical methods

In the current work, the simulation was conducted using Fluent 2021 R1, and Gambit was used to build the geometrical models and generate the mesh. This paper mainly focused on the research of the entrance region, so the grid near the inlet was refined. Meanwhile, the boundary layer mesh was built when considering the high velocity gradient and pressure gradient near the wall. Taking the elliptical microchannel with $\varepsilon = 0.5$ as an example, the grid numbers of the semi-major axis, semi-minor axis and mainstream direction are 36, 20 and 1500 respectively. Four boundary layers mesh were set in the radial direction, the first row was 0.0004, and the growth factor was 2. The growth ratio of the grid in the flow direction near the entrance was 1.014, but it was 1 near the outlet.

Based on the previous assumption, the flow and energy equations belong to the one-way coupling. Therefore, the calculation time can be effectively saved by first calculating the flow equation, followed by the energy equation. The velocity-pressure coupling problem was tackled through the application of SIMPLE algorithm. To guarantee computational accuracy, double precision solver was

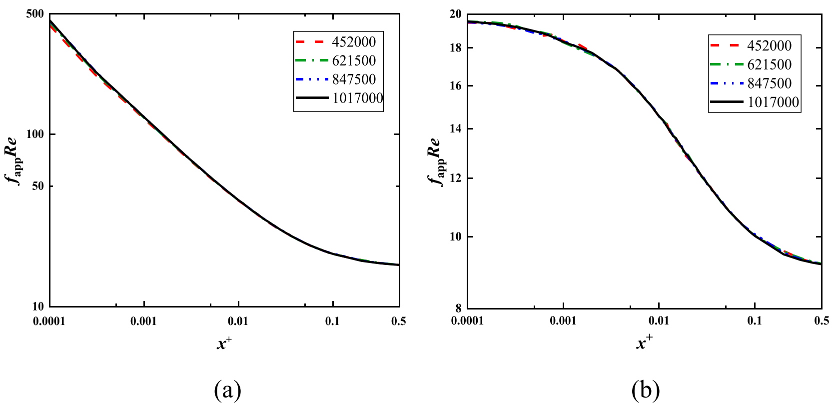

Fig. 2. $f_{\text{app}}Re$ for four different grids at $\varepsilon = 0.5$ and $Re = 1000$: (a) $Kn = 0$ and (b) $Kn = 0.1$.

chosen. Second-order upwind scheme was employed to solve the continuity and momentum equations. The residual of flow and energy equations are 10^{-9} and 10^{-12}, respectively. The velocity-slip boundary condition was embedded through user-defined functions, which have been provided in our previous work [18], and will not be further elaborated here.

3. Simulation Validation

3.1. Grid independence

In this work, the current simulation adopts the same model proposed by Su et al. [38]. Considering the complexity of the flow in the entry section, it is necessary to set up a dense grid there. We compared $f_{app}Re$ of four different grids: 452000, 621500, 847500 and 1017000, as shown in Fig. 2. When $Kn = 0$, The results near the entrance are primarily governed by the number of grids. The maximum deviation of $f_{app}Re$ is 4.1 % between the grid size of 452000 and 621500, and decreases to 2.6 % between the grid size of 621500 and 847500, Moreover, and the maximum deviation is less than 1 % between the last two grids. In addition, when $Kn = 0.1$, the calculation results indicate that the maximum deviation between each pair of grids is less than 1 %. Hence, a mesh size of 847500 is selected, which can improve computational efficiency and ensure calculation accuracy. The same steps are used to verify the grid independence for other cases.

3.2. Model validation

To validate the accuracy of present numerical results, we compare the present fRe with that in the existing work, see Fig. 3(a). Obviously, the obtained results exhibit a notable agreement with the analytical solution given by Su et al. [30], with the maximum discrepancy does not exceed 0.5 %. In addition, it is found that the present data are almost identical to that in Spiga and Vocale [34], who also numerically calculated fRe in elliptical microchannels. The above results imply that the numerical model is applicable to anticipate the results of fully developed slip-flow for elliptical microchannels.

At present, there are few available results on the slip-flow characteristics of the inlet section in the elliptic microchannel. Thus, the semi-analytical solution in Duan and Muzychka [17], and available values presented by Hornbeck [45] with tabular form are used to verify $f_{app}Re$ of the entrance region in an elliptical microchannel when the aspect ratio is 1. The deviation between the simulation results and the literature data is small when there is no slip at the entrance, and the data in the slip regime has a good consistency. The observed minor deviation might stem from the fact that the semi-analytical solution employs a linearization approximation method. The model in the present work is further verified and can be used to calculate slip-flow characteristics at the entrance region.

The present thermal resistance model is verified through a comparison of the available numerical results against existing data. Su et al. [18] presented a correlation to describe the relationship between fully developed Nu and different Kn. Haddout et al. [46] theoretically studied the microtube with uniform wall heat flux, and provided fully developed Nu in tabular form. The comparison results of fully developed Nu in this work with the above-mentioned data are presented in Tables 1 and 2, respectively, and the maximum discrepancy is less than 0.3 %.

4. Results and discussion

4.1. The flow field

In Fig. 4, the dimensionless velocity distribution at various cross-sections in the entry section of a channel is shown when $Re = 25$ and $\varepsilon = 0.5$. The overshoot phenomenon observed in the flow process is owing to the uniformity of the axial velocity profile at the inlet. This phenomenon still occurs when Kn is small because of the viscous effect. Note that the boundary layer is also gradually developing as the fluid flows along the tube. The fluid velocity outside the boundary layer remains unchanged, while the velocity of the fluid near

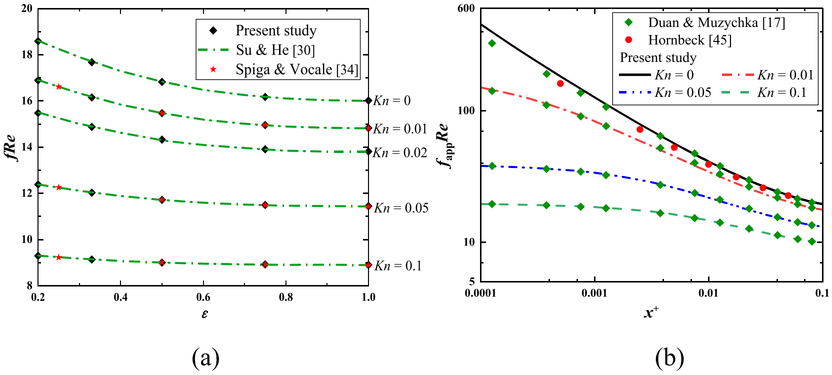

Fig. 3. Comparison of $f_{app}Re$ at $Re = 1000$ for (a) fully developed region and (b) entrance region.

Table 1
Comparison of fully developed Nu for elliptic microchannels with $\varepsilon = 1$ under T boundary condition.

Kn	This work	Su et al. [18]	%
0	3.654	3.657	0.082
0.01	3.575	3.578	0.084
0.02	3.486	3.488	0.057
0.04	3.291	3.292	0.030
0.05	3.189	3.190	0.031
0.1	2.698	2.697	0.037

Table 2
Comparison of fully developed Nu for elliptic microchannels with $\varepsilon = 1$ under H2 boundary condition.

Kn	This work	Haddout et al. [46]	%
0	4.354	4.364	0.229
0.01	4.216		
0.02	4.062	4.071	0.221
0.04	3.740	3.749	0.240
0.05	3.583		
0.1	2.898	2.904	0.207

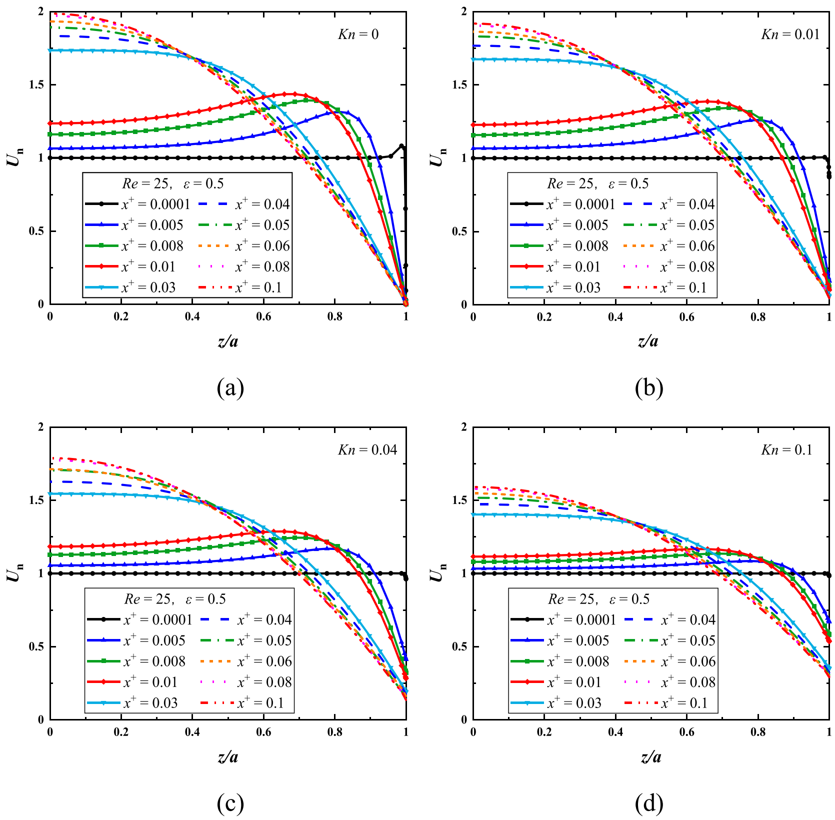

Fig. 4. Velocity profiles in an elliptic microchannel at $Re = 25$ and $\varepsilon = 0.5$: (a) $Kn = 0$, (b) $Kn = 0.01$, (c) $Kn = 0.04$ and (d) $Kn = 0.1$.

the wall is much smaller than the inlet velocity due to the viscous force, especially for the no-slip condition, as depicted in Fig. 4(a). Therefore, the fluid velocity overshoot occurs in the inlet section to satisfy the continuity equation. Meanwhile, it is apparent that the high velocity-gradient near the wall results in a high pressure-gradient, causing the velocity peak to move towards the center as x^+ increases. In slip-flow, this

phenomenon is gradually inconspicuous with increasing Kn and the velocity distribution near the entrance becomes more uniform, as shown in Fig. 4 (b)~(d). Additionally, it is obvious in Fig. 5 that when considering rarefaction effects, the velocity of the fluid close to the wall is not equal to zero, and decreases as x^+ increases. The velocity distributions are almost fully developed near $x^+ = 0.08$. It shows that the rarefaction effect will reduce the collision frequency between the fluid molecules. Based on the velocity-slip model, the decrease in velocity-gradient at the wall causes a reduction in fluid velocity at the wall.

Fig. 6 demonstrates the variation trend of the Euler number Eu along the x-axis for $\varepsilon = 0.5$ at different Re. The Euler number Eu is an important dimensionless parameter in fluid dynamics, which reflects the relative relationship of flow pressure drop with dynamic pressure in flow field and is defined as:

$$Eu = \frac{\Delta p}{\rho u_{\mathrm{m}}^2} \tag{21}$$

It is found that there is a nonlinear relationship between Eu and x^+ when $x^+ < 0.05$, while the relationship disappears when $x^+ > 0.05$. Furthermore, there is a tendency for Eu to decrease when considering the slip condition, as shown in Fig. 6(b). Notably, this decline is particularly significant when $Re < 250$. Conversely, for higher Re, the magnitude of the decrease is relatively smaller. This indicates that the slip condition exerts a more prominent drag reduction effect in microchannels with low Re. Furthermore, it can be observed that Eu decreases as Re increases, especially at $Re < 250$, where the effect of Re on Eu is prominent.

Fig. 7 depicts the axial variations of $f_{\mathrm{app}}Re$ for the elliptical microchannels with different Re at $Kn = 0$ and 0.1. Obviously, $f_{\mathrm{app}}Re$ gradually decreases with increasing Re at the entrance region. It shows that the higher the Re, the better the flow performance. For no-slip flow, the effect of Re on $f_{\mathrm{app}}Re$ is particularly significant when $Re < 500$. For slip-flow, the Knudsen number can significantly reduce the effect of Re, especially at large Kn. It can be proven by the velocity distribution in Fig. 4, as it clearly illustrates that the velocity-gradient decreases significantly at high Knudsen numbers, particularly in the inlet section. Furthermore, it can be found that $f_{\mathrm{app}}Re$ of the hydrodynamic entry region far exceeds that of the fully developed, and $f_{\mathrm{app}}Re$ value sharply decreases when the dimensionless axial distance increases from 0.0001 to 1. After reaching the FDR, $f_{\mathrm{app}}Re$ of different Re approaches a constant value, indicating that $f_{\mathrm{app}}Re$ of fully developed flow is irrelevant to Re. It highlights the important role of Re in the flow performance of the entry section, which indicates that the influence of Re cannot be ignored in microchannels regardless of slip or no-slip flows, especially for short channels.

Fig. 8 shows the axial variation of $f_{\mathrm{app}}Re$ for different channel aspect ratios. Likewise, for various ε, $f_{\mathrm{app}}Re$ at the entrance substantially exceeds that in the FDR. Notably, the deviation of $f_{\mathrm{app}}Re$ among different ε is minor near the inlet, especially when the rarefaction effect is ignored (i.e., $Kn = 0$), where the curves almost overlap. Therefore, the influence of the cross-section shape on $f_{\mathrm{app}}Re$ can be almost neglected at the inlet. However, it is apparent that the deviation gradually increases with x^+ until it reaches its maximum and remains essentially unchanged at the FDR. This indicates that the fully developed $f_{\mathrm{app}}Re$ has always been affected by ε and cannot be overlooked, especially as ε decreases, and its effect increases further.

Fig. 9 illustrates the development of $f_{\mathrm{app}}Re$ for elliptical microchannels along axial distances with different Kn at $Re = 50$ and $Re = 500$. As shown in Fig. 4, the rarefaction effect flattens the velocity distribution and reduces the velocity-gradient, which further reduces the friction factor. Therefore, $f_{\mathrm{app}}Re$ gradually decreases with increasing Kn. Meanwhile, it can be found that when Kn increases from 0 to 0.01, $f_{\mathrm{app}}Re$ near the entrance decreases sharply, and then $f_{\mathrm{app}}Re$ declines slowly with Kn along the axial direction. At $x^+ = 0.0001$, the reduction of $f_{\mathrm{app}}Re$ from $Kn = 0$ to $Kn = 0.01$ is approximately 94.6 % and 75 % in Fig. 9 (a) and (b) respectively. It demonstrates that even a slight slip can considerably reduce friction resistance in the entry section. What's more, it also shows that when Re is small, the impact of Kn on f increases further, which aligns with the observation in Fig. 6. At the inlet, when Kn increases from 0.01 to 0.1, $f_{\mathrm{app}}Re$ is decreased by 88.9 % and 87.1 % at $Re = 50$ and $Re = 500$, respectively. Note that the deviation of $f_{\mathrm{app}}Re$ near the inlet for different Re gradually drops with the increase of Kn, and the divergence shown in Fig. 9 is less than 0.3 when $Kn = 0.1$, which is almost negligible.

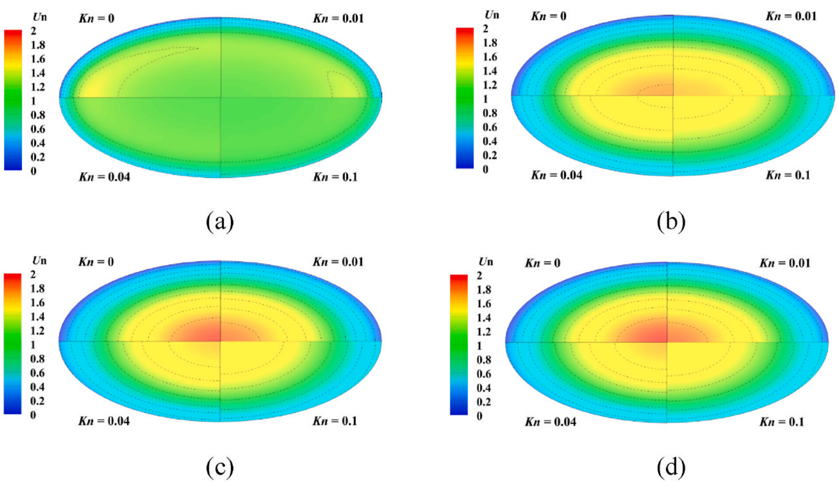

Fig. 5. Dimensionless velocity contours at $Re = 25$ and $\varepsilon = 0.5$: (a) $x^+ = 0.005$, (b) $x^+ = 0.04$, (c) $x^+ = 0.08$ and (d) $x^+ = 0.1$.

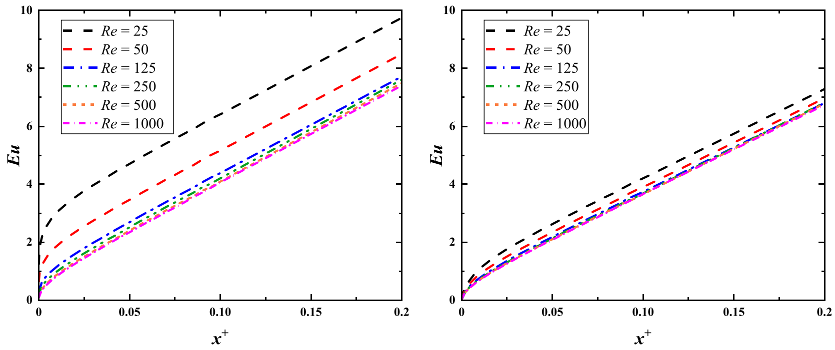

(a) (b)

Fig. 6. Distribution of Eu at different Re for $\varepsilon = 0.5$: (a) $Kn = 0$ and (b) $Kn = 0.01$.

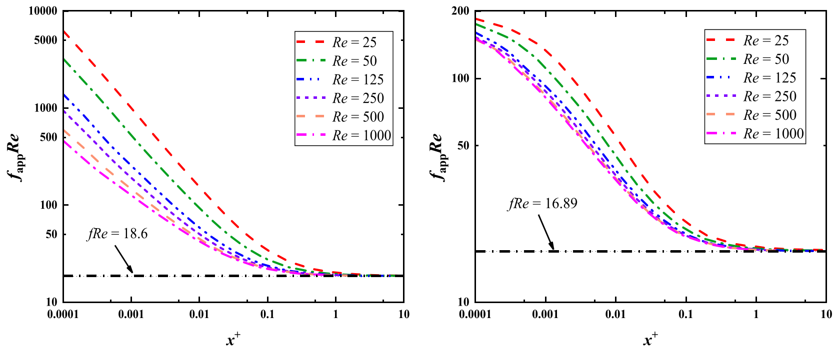

(a) (b)

Fig. 7. Axial variation of $f_{app}Re$ at different Re for $\varepsilon = 0.2$: (a) $Kn = 0$ and (b) $Kn = 0.1$.

4.2. The temperature field

Figs. 10 and 11 illustrate the dimensionless temperature profiles corresponding to four different axial locations for $Pe = 35$ and $\varepsilon = 0.5$ under T and H2 boundaries, respectively. It can be observed that when $Kn = 0$, the temperature distributions at $x^* = 0.001$ between T and H2 boundaries are not much different, indicating that the temperature distribution near the inlet is almost unaffected by these two boundaries. However, as x^* gradually increases, significant differences in temperature distribution emerge between the two boundary conditions. It is worth noting that the temperature-jump causes a deviation between the temperature of the fluid near the wall and the wall temperature when contrasting with the no-slip and no-jump. A higher Kn results in a significant jump in temperature, generating a contact thermal resistance effect. This, in turn, triggers the decline of heat transfer rate at the wall, resulting in a decrease in fluid temperature. Similar findings can be found in Ref. [18,47,48]. As illustrated in Figs. 10 and 11, the rarefaction effect becomes more apparent at the constant wall temperature, especially for high Kn. In addition, at any axial position of an elliptical microchannel, the fluid temperature close to the center of flow is less impacted by Kn, particularly for H2 boundary condition, while its effect becomes significant close to the wall. Furthermore, the fluid temperature reaches the minimum at the channel center and peaks at the terminus of the semi-major axis in H2 condition.

Fig. 12 depicts the axial variation of $Nu(x)$ in an elliptic microchannel for different Pe at $\varepsilon = 0.75$. Notably, $Nu(x)$ is relatively large near the inlet owing to the thinness of thermal boundary layer. As increasing x^*, $Nu(x)$ near the thermal entry region shows a monotonically decreasing trend until it reaches the asymptotic value of its fully developed regime. It should be pointed out that compared with H2 boundary condition, Pe has a significantly greater impact on $Nu(x)$ at the entrance section

under T boundary condition especially for no-slip case. For T boundary, when Pe changes from 17.5 to 350, $Nu(x)$ is decreased by 87 % at $x^* = 0.0001$. While the value is 67 % for H2 condition. Besides, the value of $Nu(x)$ for $Kn = 0.04$ is reduced by 333 and 176 when compared with the no-slip case under T and H2 boundary conditions, respectively. Therefore, the influence of Pe cannot be overlooked when near the entrance. Nevertheless, in the thermal entry region, as Kn increases, the difference in $Nu(x)$ for various Pe diminishes significantly under different thermal boundary conditions. This is due the fact that AHC depends on the heat conduction of molecules. While the gas becomes thinner as increasing Kn, which reduces the collision between molecules, resulting in the heat transfer is deteriorated. It is more apparent in the entrance region where the effect of AHC on heat transfer is significant. This indicates

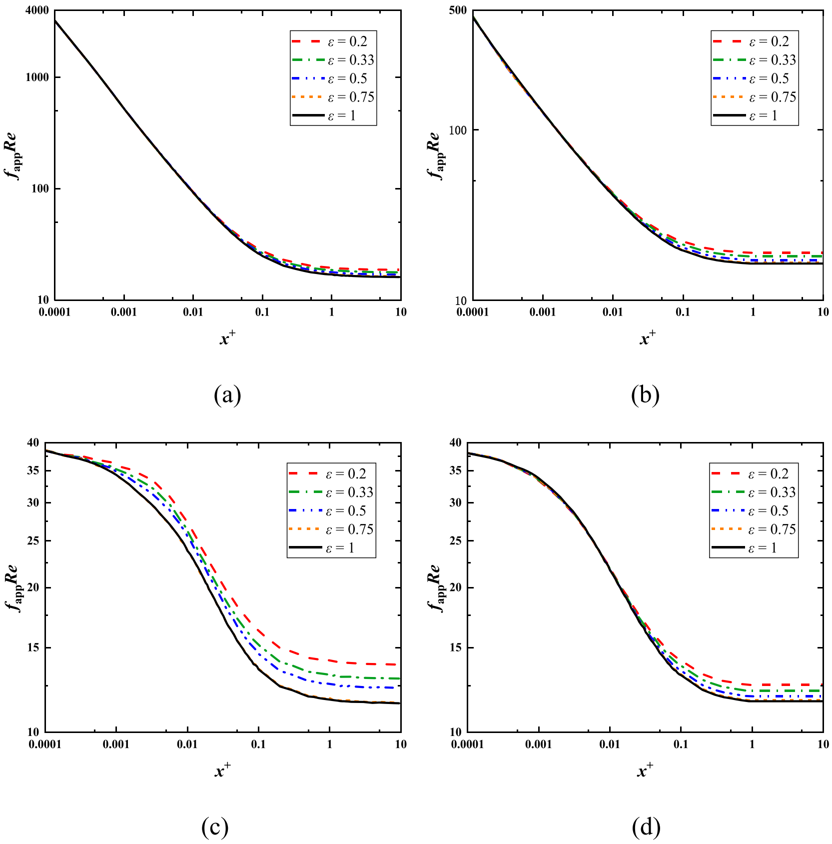

Fig. 8. Axial variation of $f_{app}Re$ for different ε under $Kn = 0$ with (a) $Re = 50$, (b) $Re = 1000$; and under $Kn = 0.05$ with (c) $Re = 50$, (d) $Re = 1000$.

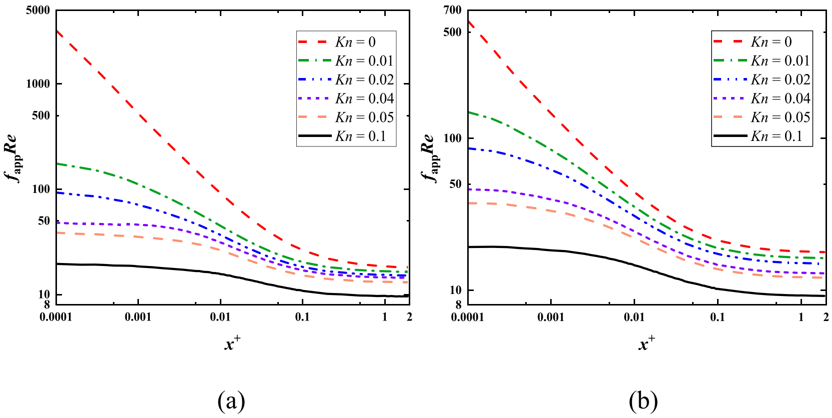

Fig. 9. Axial variation of $f_{app}Re$ at different Kn for $\varepsilon = 0.33$: (a) $Re = 50$ and (b) $Re = 500$.

that rarefaction weakens the role of AHC on thermal transfer at the entrance region.

The impact of Kn on $Nu(x)$ under T and H2 boundaries is illustrated in Fig. 13. It is evident that temperature-jump significantly reduces the rate of heat transfer, especially for thermal entry region. A recent study on trapezoidal microchannels [49], it also shows that deterioration effect caused by temperature-jump holds sway in the heat transfer process. Therefore, increasing Kn reduces heat transfer. Like the effect of Kn on $f_{app}Re$, the impact of Kn on $Nu(x)$ fades away with x^* growth and gradually disappears as it reaches thermally fully developed region. When Kn rises from 0 to 0.01, the rarefaction effect is more pronounced near the inlet under H2 boundary condition, where $Nu(x)$ decreases by approximately 45.4 % in contrast to the no-slip at $\varepsilon = 0.33$. The reduction is relatively smaller (around 28 %) for T boundary. Notably, for slip-flow, $Nu(x)$ near the inlet is nearly identical for T and H2 boundaries. It indicates that the heat transfer at the inlet is almost independent of these two thermal boundaries. Additionally, it is found that the

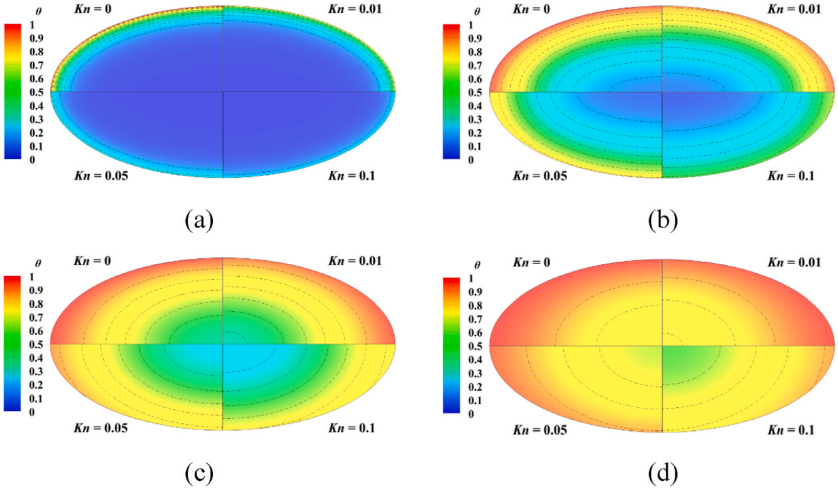

Fig. 10. Dimensionless temperature contours at $Pe = 35$ for $\varepsilon = 0.5$ under T boundary condition: (a) $x^* = 0.001$, (b) $x^* = 0.015$, (c) $x^* = 0.05$ and (d) $x^* = 0.1$.

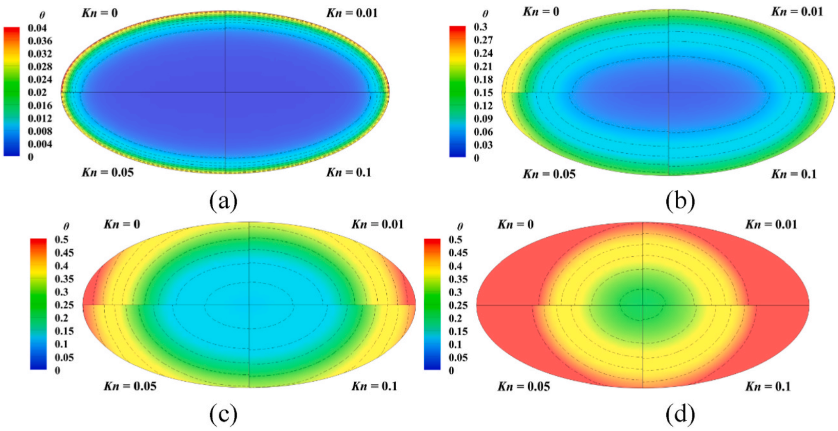

Fig. 11. Dimensionless temperature contours at $Pe = 35$ for $\varepsilon = 0.5$ under H2 boundary condition: (a) $x^* = 0.001$, (b) $x^* = 0.015$, (c) $x^* = 0.05$ and (d) $x^* = 0.1$.

discrepancy of $Nu(x)$ with different ε is minimal close to the inlet. In other words, the geometric shape cannot be identified as the fluid is about to ingress an elliptic channel.

Fig. 14 depicts the variation of $Nu(x)$ with increasing axial dimensionless distance x^* at various ε for $Kn = 0.01$ and $Kn = 0.1$. Likewise, it is visible from Fig. 14 that $Nu(x)$ close to the inlet is independent of geometric shape. For T boundary condition, $Nu(x)$ decreases with increasing ε in the transition region, that is, the section situated between the entrance and the fully developed regions. However, as Kn increases, the impact of ε on fully developed Nu becomes apparent, which is opposite to that in the transition region. It can be ascribed that as the aspect ratio decreases, the channel shape becomes flatter, which usually leads to an increase in heat flux, but the increase of Kn reduces heat transfer, resulting in a decrease in the net heat transfer rate. Clearly, in the FDR, the aspect ratio's impact on $Nu(x)$ fades away. For H2 boundary condition, the influence of ε is primarily reflected in the FDR where $Nu(x)$ decreases sharply with decreasing ε, indicating a longer thermal entry length for lower ε. Furthermore, it is noteworthy that for same Kn, the aspect ratio exerts a more pronounced influence on the fully developed Nu with H2 condition. This may be related to the local high temperature at the end of the major semi-axis under H2 conditions, which will deteriorate the convective heat transfer and are more pronounced in channels with a relatively small ε. As anticipated, $Nu(x)$ is significantly influenced by aspect ratio in transition and fully developed regions. It may be stem from the fact that at the inlet, the influence of geometry on heat transfer performance has not been aware. While as the fluid flows along the elliptical channel, the impact of channel geometry on thermal performance becomes apparent. In other words, the heat transfer characteristic at the inlet of an elliptical microchannel can be replaced by another channel with different ε.

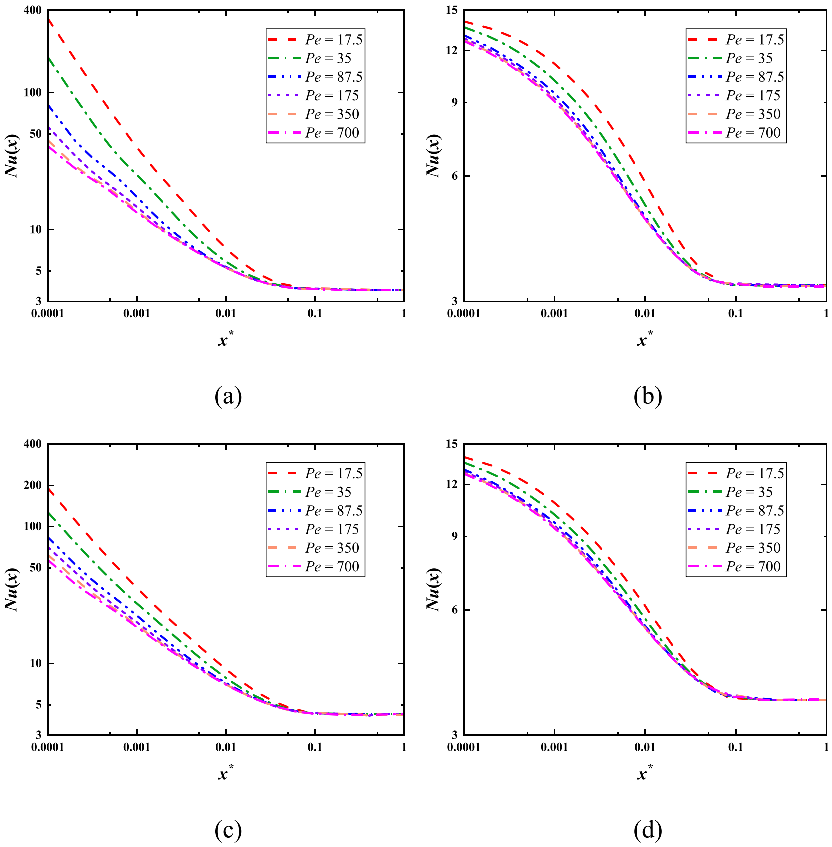

Fig. 12. Axial variation of $Nu(x)$ in different Pe for $\varepsilon = 0.75$ under T boundary condition with (a) $Kn = 0$, (b) $Kn = 0.04$; and under H2 boundary condition with (c) $Kn = 0$, (d) $Kn = 0.04$.

4.3. Correlations

The slip-flow and heat transfer characteristics at the entry section in the elliptic microchannel are affected by numerous complex factors, such as Kn, ε, Pe, and x^*, making it difficult to accurately describe using a concise correlation. But it is available in the FDR. Fig. 15 displays the impacts of both ε and Kn on the fully developed Nu. For T boundary condition, the fully developed Nu reduces as increasing Kn, which is primarily owing to the change of temperature-jump. Additionally, the influence of ε on fully developed Nu is small and it exhibits irregular tendency, particularly for low Knudsen number where its impact is nearly negligible. However, a different phenomenon occurs for H2 boundary condition. As ε increases, the fully developed Nusselt number gradually rises, implying that the augmentation of ε enhances heat transfer efficiency under H2 boundary. It is noteworthy that when the aspect ratio is in the range of 0.2–0.5, the augmentation in the fully developed Nu is particularly remarkable. Meanwhile, the influence of ε on Nu is more pronounced when Kn is small. What's more, the Nusselt number has an intriguing trend. Nu initially increases and then diminishes as rising Kn at $\varepsilon = 0.2$, whereas this non-monotonic trend is absent at other aspect ratios.

For fully developed flow, Vocale et al. [35] proposed a correlation for Nu with H2 condition based on numerical simulations. However, the applicability is limited in practical application due to the involvement of numerous parameters and each operating condition corresponding to a set of parameters. Nu is relatively sensitive to the variation of ε and Kn, but unrelated to Pe from the numerical results. Therefore, correlations for Nu have been derived in T and H2 conditions through surface fitting with the present results, as shown in Eqs. (22) and (23). The applicable range of these equations is $0.01 \le Kn \le 0.1$ and $0.2 \le \varepsilon \le 1$. Compared to the numerical results, the accuracy of these correlations is presentable since the relative error is within 1 %.

$$(Nu)_{\mathrm{T}} = \frac{3.563 + 7.933\varepsilon - 10.16\varepsilon^2 + 4.641\varepsilon^3 - 1.37\varepsilon^4 - 7.578\varepsilon Kn}{1 + 1.588\varepsilon + 7.051Kn - 1.327\varepsilon^2 + 8.842Kn^2 - 6.251\varepsilon Kn} \tag{22}$$

$$(Nu)_{\mathrm{H2}} = \frac{-3.037 + 32.347\varepsilon + 17.52Kn - 45.698Kn^2 - 80\varepsilon Kn}{1 + 4.097\varepsilon - 2.821Kn + 1.597\varepsilon^2 + 14.179\varepsilon Kn} \tag{23}$$

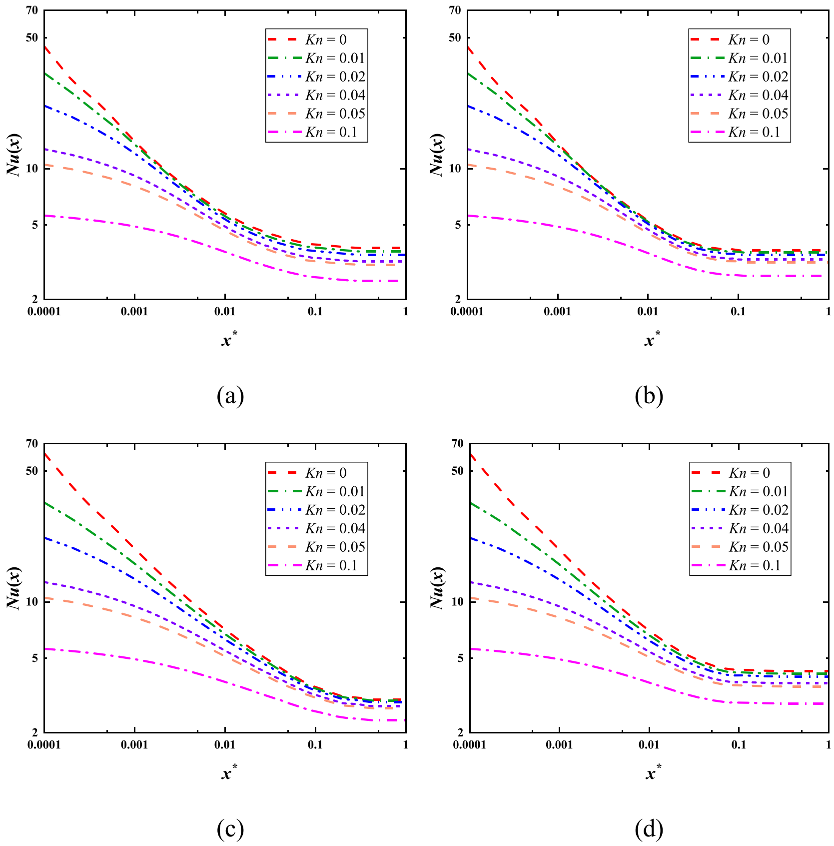

Fig. 13. Axial variation of $Nu(x)$ in different Kn for $Pe = 350$ under T boundary condition with (a) $\varepsilon = 0.33$, (b) $\varepsilon = 0.75$; and under H2 boundary condition with (c) $\varepsilon = 0.33$, (d) $\varepsilon = 0.75$.

5. Conclusions

In this paper, numerical simulations are conducted to investigate the slip-flow and heat transfer characteristics at the entrance region of elliptic microchannels under T and H2 boundary conditions. The impacts of the Reynolds number, Knudsen number, Peclet number and aspect ratio on $f_{app}Re$ and $Nu(x)$ are discussed. The main conclusions are addressed as follows:

[1] $f_{app}Re$ decreases with increasing Re. When $\varepsilon = 0.33$, $Kn = 0.01$ and $Re < 500$, the effect of Re on $f_{app}Re$ is particularly significant at the entrance, decreasing gradually along the flow direction until it reaches a constant value in FDR. The effect of Pe on $Nu(x)$ shows a similar trend.

[2] The rarefaction effect significantly reduces friction factor f in the entrance section of an elliptical microchannel. Specifically, when $\varepsilon = 0.33$, $Kn = 0.01$ and $Re = 50$, $f_{app}Re$ at the inlet is about 94.6 % of the no-slip condition. However, $f_{app}Re$ is decreased by 88.9 % when Kn increases from 0.01 to 0.1.

[3] Axial heat conduction enhances the heat transfer capacity of the inlet section, but the rarefaction diminishes the effect. At $\varepsilon = 0.75$ and $x^* = 0.0001$, when Pe ranges from 17.5 to 350, $Nu(x)$ is decreases by 87 % at the T boundary. The value of $Nu(x)$ for $Kn = 0.04$ is reduces by 333 when compared with no-slip case at Pe is 17.5. When $Pe > 350$, the effect is negligible. In addition, fully developed Nu is independent of Pe and decreases with Kn.

[4] The impact of channel geometry on $f_{app}Re$ and $Nu(x)$ can be neglected close to the inlet. But the friction and heat transfer coefficients exhibit a larger sensitivity to the ε near the FDR, particularly for H2 boundary. Besides, fully developed Nu decreases with increasing ε at $Kn \neq 0$.

[5] Correlations of the fully developed Nu are developed considering the impacts of ε and Kn with the relative error of 1 %.

To sum up, the study of the entrance region of elliptical microchannels reveals the effects of slip boundaries, channel aspect ratios, axial heat conduction, and Reynolds number on flow and heat transfer. Although there are some limitations, this numerical work can be used to optimize the design of microchannel heat sinks. In addition, the investigation of mixed convection in elliptical microchannels, especially those areas that are rarely studied, such as the inlet region, different inclinations or rotation angles, is also an important point of view, which should be considered in future works.

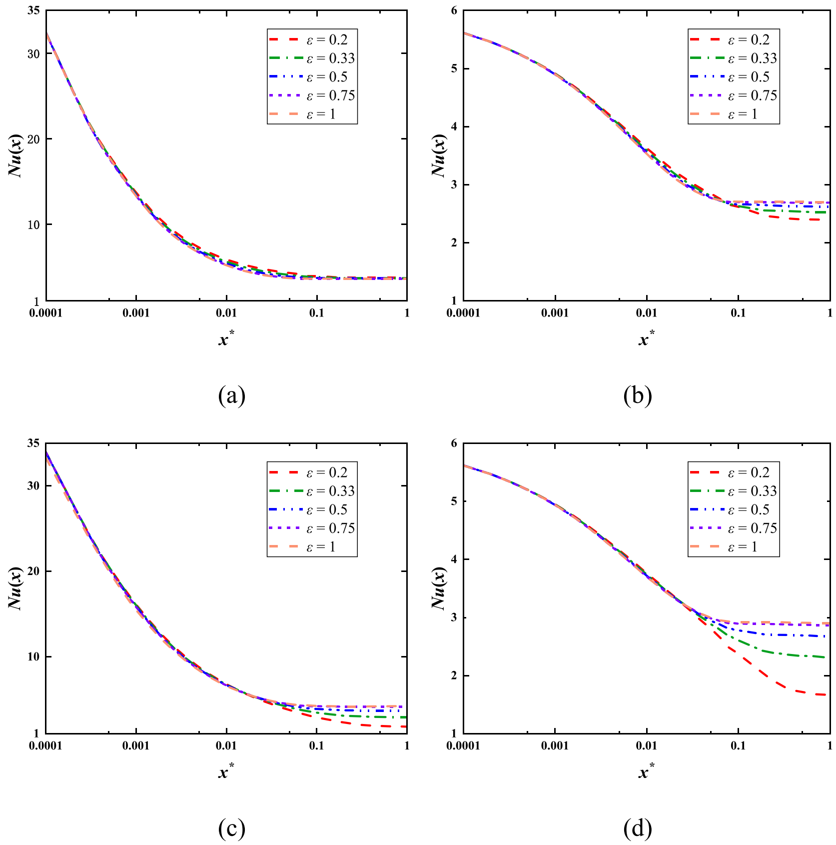

Fig. 14. Axial variation of $Nu(x)$ in different ε for $Pe = 350$ under T boundary condition with (a) $Kn = 0.01$, (b) $Kn = 0.1$; and under H2 boundary condition with (c) $Kn = 0.01$, (d) $Kn = 0.1$.

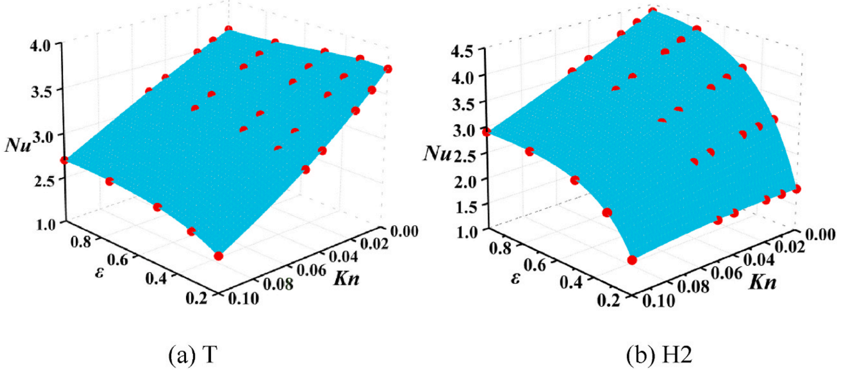

Fig. 15. Variation of fully developed Nu versus ε for different Knudsen numbers.

CRediT authorship contribution statement

Liangbin Su: Writing – review & editing, Methodology, Funding acquisition, Conceptualization. **Yongyi Yang:** Writing – original draft, Validation, Methodology, Data curation. **Liang Li:** Funding acquisition. **Wan Yu:** Funding acquisition. **Huashan Su:** Formal analysis. **Gang Wang:** Validation. **Tao Hu:** Writing – review & editing.

Declaration of competing interest

The authors declare that they have no known competing financial interests or personal relationships that could have appeared to influence the work reported in this paper.

Acknowledgments

This work was financially supported by Chunhui Plan Collaborative Research Project of Ministry of Education (No. HZKY20220343), the Opening Foundation of Hubei Key Laboratory of Hydroelectric Machinery Design & Maintenance (No. 2023KJX05), and International Science and Technology Cooperation Project of Hubei Province (No. 2023EHA016). The authors acknowledge support from the Brunel University London BRIEF award and the Royal Society Research Grant (RGS\R2\222256).

Data availability

Data will be made available on request.

References

[1] D.B. Tuckerman, R.F.W. Pease, High-performance heat sinking for VLSI, IEEE Electron. Device Lett. 2 (5) (1981) 126–129.
[2] A. Abedini, S. Ahitan, Z. Barikbin, V. Soni, J. Ratulowski, D. Sinton, Past, present, and future of microfluidic fluid analysis in the energy industry, Energy Fuels 36 (16) (2022) 8578–8590.
[3] A. Shahsavar, K. Moradi, Ç. Yıldız, P. Farhadi, M. Arıcı, Effect of nanoparticle shape on cooling performance of boehmite-alumina nanofluid in a helical heat sink for laminar and turbulent flow regimes, Int. J. Mech. Sci. 217 (2022) 107045.
[4] H. Adam, S.C.B. Gopinath, M.K. Md Arshad, T. Adam, U. Hashim, Z. Sauli, M.A. Fakhri, S. Subramaniam, Y. Chen, S. Sasidharan, Y.S. Wu, Integration of microfluidic channel on electrochemical-based nanobiosensors for monoplex and multiplex analyses: an overview, J. Taiwan Inst. Chem. Eng. 146 (2023) 104814.
[5] Z. Duan, Y.S. Muzychka, Slip flow in elliptic microchannels, Int. J. Therm. Sci. 46 (11) (2007) 1104–1111.
[6] S.G. Kandlikar, W.J. Grande, Evolution of microchannel flow passages–thermohydraulic performance and fabrication technology, Heat Tran. Eng. 24 (1) (2003) 3–17.
[7] S.S. Mehendale, A.M. Jacobi, R.K. Shah, Fluid flow and heat transfer at micro- and meso-scales with application to heat exchanger design, Appl. Mech. Rev. 53 (7) (2000) 175–193.
[8] A.A. Avramenko, Yu Yu Kovetska, I.V. Shevchuk, A.I. Tyrinov, V.I. Shevchuk, Mixed convection in vertical flat and circular porous microchannels, Transport Porous Media 124 (3) (2018) 919–941.
[9] A.A. Avramenko, A.I. Tyrinov, I.V. Shevchuk, N.P. Dmitrenko, A.V. Kravchuk, V.I. Shevchuk, Mixed convection in a vertical flat microchannel, Int. J. Heat Mass Tran. 106 (2017) 1164–1173.
[10] H.-S. Kou, J.-J. Lee, C.-W. Chen, Optimum thermal performance of microchannel heat sink by adjusting channel width and height, Int. Commun. Heat Mass Tran. 35 (5) (2008) 577–582.
[11] G.L. Morini, M. Spiga, P. Tartarini, The rarefaction effect on the friction factor of gas flow in microchannels, Superlattice. Microst. 35 (3–6) (2004) 587–599.
[12] Z.-Y. Guo, Z.-X. Li, Size effect on microscale single-phase flow and heat transfer, Int. J. Heat Mass Tran. 46 (2003) 149–159.
[13] N.-T. Nguyen, S.T. Wereley, S.A.M. Shaegh, Fundamentals and Applications of Microfluidics, Artech House, Norwood, Massachusetts, 2019.
[14] M. Renksizbulut, H. Niazmand, G. Tercan, Slip-flow and heat transfer in rectangular microchannels with constant wall temperature, Int. J. Therm. Sci. 45 (9) (2006) 870–881.
[15] A.A. Avramenko, A.I. Tyrinov, I.V. Shevchuk, Start-up slip flow in a microchannel with a rectangular cross section, Theor. Comput. Fluid Dynam. 29 (5–6) (2015) 351–371.
[16] A.A. Avramenko, A.I. Tyrinov, I.V. Shevchuk, Theoretical investigation of steady isothermal slip flow in a curved microchannel with a rectangular cross-section and constant radii of wall curvature, Eur. J. Mech. - BFluids 54 (2015) 87–97.
[17] Z. Duan, Y.S. Muzychka, Slip flow in the hydrodynamic entrance region of circular and noncircular microchannels, J. Fluid Eng. 132 (1) (2010) 011201.
[18] L. Su, B. He, G. Wang, R. Xiao, W. Yu, Simultaneously developing flow and heat transfer in circular and parallel-plates microchannels with velocity slip and temperature jump, Int. J. Therm. Sci. 177 (2022) 107590.
[19] O. Aydin, M. Avci, Laminar forced convective slip flow in a microduct with a sinusoidally varying heat flux in axial direction, Int. J. Heat Mass Tran. 89 (2015) 606–612.
[20] M. Avci, O. Aydin, Analysis of extended micro-graetz problem in a microtube, Sādhanā 43 (7) (2018) 105.
[21] H.A. Mohammed, P. Gunnasegaran, N.H. Shuaib, The impact of various nanofluid types on triangular microchannels heat sink cooling performance, Int. Commun. Heat Mass Tran. 38 (6) (2011) 767–773.
[22] C.Y. Wang, Benchmark solutions for slip flow and H1 heat transfer in rectangular and equilateral triangular ducts, J. Heat Tran. 135 (2) (2013) 021703.
[23] H. Nemati, M.A. Moghimi, C.N. Markides, Heat transfer characteristics of thermally and hydrodynamically developing flows in multi-layer mini-channel heat sinks, Int. J. Heat Mass Tran. 208 (2023) 124052.
[24] W.A. Khan, M.M. Yovanovich, Models and correlations for rarefied gas flows in polygonal and trapezoidal microducts, J. Thermophys. Heat Tran. 34 (2) (2020) 296–303.
[25] J. Song, F. Liu, Y. Sui, D. Jing, Numerical studies on the hydraulic and thermal performances of trapezoidal microchannel heat sink, Int. J. Therm. Sci. 161 (2021) 106755.
[26] U. Manda, S. Mazumdar, Y. Peles, Effects of cross-sectional shape on flow and heat transfer of the laminar flow of supercritical carbon dioxide inside horizontal microchannels, Int. J. Therm. Sci. 201 (2024) 108992.
[27] M. Shams, M. Shojaeian, C. Aghanajafi, S.A.R. Dibaji, Numerical simulation of slip flow through rhombus microchannels, Int. Commun. Heat Mass Tran. 36 (10) (2009) 1075–1081.
[28] S.D. Farahani, A.J. Mamoei, A. Alizadeh, Thermal performance of microchannel heat sink integrated with porous medium, slip coefficient and phase change material and machine learning approach, J. Energy Storage 74 (2023) 109357.
[29] D. Jing, S. Song, Y. Pan, X. Wang, Size dependences of hydraulic resistance and heat transfer of fluid flow in elliptical microchannel heat sinks with boundary slip, Int. J. Heat Mass Tran. 119 (2018) 647–653.
[30] L. Su, B. He, X. Wu, F. Hong, Analytical solutions of slip flow and H1 heat transfer in elliptical microchannels, Int. J. Therm. Sci. 184 (2023) 108017.
[31] H. Ragueb, K. Mansouri, An analytical study of the periodic laminar forced convection of non-Newtonian nanofluid flow inside an elliptical duct, Int. J. Heat Mass Tran. 127 (2018) 469–483.
[32] R. Deepakkumar, S. Jayavel, Air side performance of finned-tube heat exchanger with combination of circular and elliptical tubes, Appl. Therm. Eng. 119 (2017) 360–372.
[33] R.K. Shah, A.L. London, Laminar Flow Forced Convection in Ducts: A Source Book for Compact Heat Exchanger Analytical Data, Academic Press, New York, 1978.
[34] M. Spiga, P. Vocale, Slip flow in elliptic microducts with constant heat flux, Adv. Mech. Eng. 4 (2012) 481280.
[35] P. Vocale, G.L. Morini, M. Spiga, Dilute gas flows through elliptic microchannels under H2 boundary conditions, Int. J. Heat Mass Tran. 71 (2014) 376–385.

[36] S.K. Das, F. Tahmoure, Analytical solution of fully developed gaseous slip flow in elliptic microchannel, Int. J. Adv. Appl. Math. Mech. 3 (3) (2016) 1–15.

[37] A. Bhosale, S.Y. Bhosale, H.N. Deshpande, S.K. Saha, Laminar forced convective heat transfer performance analysis of elliptical and semicircular microchannels, J. Thermophys. Heat Tran. 36 (4) (2022) 836–847.

[38] L. Su, Z. Duan, B. He, H. Ma, G. Ding, Laminar flow and heat transfer in the entrance region of elliptical minichannels, Int. J. Heat Mass Tran. 145 (2019) 118717.

[39] F. Yu, T. Wang, C. Zhang, Effect of axial conduction on heat transfer in a rectangular microchannel with local heat flux, J. Therm. Sci. Technol. 13 (1) (2018). JTST0013–JTST0013.

[40] I. Mitra, I. Ghosh, Analytical closed-form solution for fluid flow through microchannel heat sinks including axial conduction, Int. Commun. Heat Mass Tran. 129 (2021) 105732.

[41] M. Gad-el-Hak, The fluid mechanics of microdevices—the freeman scholar lecture, J. Fluid Eng. 121 (1) (1999) 5–33.

[42] O. Aydın, M. Avcı, Heat and fluid flow characteristics of gases in micropipes, Int. J. Heat Mass Tran. 49 (9–10) (2006) 1723–1730.

[43] W.M. Rohsenow, H.Y. Choi, Heat, mass and momentum transfer, J. R. Aeronaut. Soc. 66 (618) (1961), 405–405.

[44] T.L. Bergman, A.S. Lavine, F.P. Incropera, D.P. Dewitt, in: Fundamentals of Heat and Mass Transfer, seventh ed., John Wiley & Sons, New York, 2011.

[45] R.W. Hornbeck, Laminar flow in the entrance region of a pipe, Appl. Sci. Res. 13 (1) (1964) 224–232.

[46] Y. Haddout, E. Essaghir, A. Oubarra, J. Lahjomri, Convective heat transfer for a gaseous slip flow in micropipe and parallel-plate microchannel with uniform wall heat flux: effect of axial heat conduction, Indian J. Phys. 92 (6) (2018) 741–755.

[47] X. Zhu, Analysis of heat transfer between two unsymmetrically heated parallel plates with microspacing in the slip flow regime, Microscale Thermophys. Eng. 6 (4) (2003) 287–301.

[48] F. Xu, H. Ma, Analytical solution of the graetz problem extended to slip-flow in microtube, J. Heat Tran. 134 (10) (2012) 104501.

[49] H. Niazmand, M. Renksizbulut, E. Saeedi, Developing slip-flow and heat transfer in trapezoidal microchannels, Int. J. Heat Mass Tran. 51 (25–26) (2008) 6126–6135.